REVISTA MATÉRIA V.30
ISSN 1517-7076 articles e20250706, 2025

# Influence mechanism of termination voltage on the microstructure and corrosion resistance of micro-arc oxidation coatings on AZ31B magnesium alloy

Yiming Sun[1], Chongchong Li[1], Haichao Zhao[2], Kaipeng Zhang[1], Renying Liu[1], Xiangqian Wei[1], Zean Zhang[1], Yue Chang[1]

[1]North China Institute of Aerospace Engineering, School of Materials Engineering. Langfang, Hebei, China.

[2]Army Academy of Armored Forces, National Engineering Research Center for Remanufacturing. Beijing, China.

e-mail: 17663061692@163.com, hgdlichong@163.com, zhchebei@sina.com, zkp20010125@163.com, 972872127@qq.com, 820562121@qq.com, 120947537@qq.com, 2236057747@qq.com

## ABSTRACT

This study investigates the impact of voltage on the microstructure and corrosion resistance of AZ31B magnesium alloy micro-arc oxidation (MAO) coating. Coatings were prepared at voltages of 300 V, 350 V, 400 V, and 450 V, and their performance was systematically analyzed using scanning electron microscopy (SEM), X-ray diffraction (XRD), electrochemical testing, contact angle measurement, and hardness testing. The findings reveal that as the voltage increases, the coating thickness initially increases before stabilizing, while the surface porosity decreases initially but increases subsequently. The lowest porosity and highest compactness are observed at 350 V. The primary phases of the coating are MgO and $Mg_2SiO_4$, with higher voltage promoting the formation of MgO. Hardness and roughness exhibit an initial increase followed by a decrease. Electrochemical tests indicate that the 350 V coating has the lowest corrosion current density, the highest impedance modulus, and the best corrosion resistance. Excessive voltage leads to crack formation on the coating surface, compromising its integrity and corrosion resistance. The study concludes that 350 V optimizes the compactness, phase composition, and surface morphology of the coating, thereby enhancing its corrosion resistance. This provides experimental evidence for optimizing surface protection processes for magnesium alloys.

**Keywords:** AZ31B magnesium alloy; Micro-arc oxidation; Termination voltage; Microstructure; Corrosion resistance.

## 1. INTRODUCTION

Magnesium alloys, celebrated for their lightweight structural advantages, are widely hailed as the green structural materials of the 21st century. Their appeal stems from superior specific strength, excellent thermal conductivity, and remarkable biocompatibility, rendering them highly promising in aerospace, automotive, and biomedicine [1–4]. Nonetheless, the inherently low standard electrode potential of magnesium predisposes it prone to corrosion, severely limiting its practical applications [5, 6]. For this reason, enhancing the corrosion resistance of Mg alloys is one of the most critical challenges for materials scientists and engineers. Currently, various surface modification strategies are being explored to address this challenge. These include the development of protective coatings such as sol-gel derived bioglass [7] and the fabrication of particle-reinforced metal matrix composites like $ZrB_2$/AZ64 [8]. Additionally, understanding the microstructural evolution of magnesium alloys under thermal processing, as investigated in laser welding studies of AZ31B and cerium-containing alloys [9, 10], provides valuable insights into material behavior under high-energy input conditions, which is relevant to processes like micro-arc oxidation (MAO).

Among the various surface treatment methodologies, MAO stands out as one of the most effective and efficient methods for corrosion protection of Mg alloy, because of its green and easy process, which imparts a robust, ceramic coating that adheres tenaciously to the magnesium alloy substrate, thereby offering enhanced protection against corrosion [11–15].

The performance of micro-arc oxidation (MAO) coatings is contingent upon numerous factors, including electrolyte composition, treatment duration, current density, and voltage. Among these variables, voltage stands out as a pivotal determinant in modulating the structure and performance of the coating [16]. The voltage dictates

Corresponding Author: Chongchong Li Received on 19/08/2025 Accepted on 03/11/2025

DOI: https://doi.org/10.1590/1517-7076-RMAT-2025-0706

the intensity of plasma discharge, which in turn influences the growth rate, porosity, and phase composition of the MAO coating. At lower voltages, the discharge intensity is subdued, culminating in a thinner coating characterized by increased porosity. These pores are formed due to the eruption channels of molten oxide during micro-arc generation, or through the pressurized ejection of air bubbles that are encapsulated in the oxide film during coating formation [17–19]. Conversely, at elevated voltages, the discharge is more vigorous, potentially leading to the cracking of the coating [20]. Studies have demonstrated that the corrosion resistance of MAO coatings formed on AZ31B magnesium alloy at varying voltages exhibits marked disparities. Nevertheless, the underlying mechanism connecting voltage to the microstructure and corrosion resistance of the coating warrants further investigation [21].

In recent years, a series of studies have been conducted on the influence of voltage on MAO coatings. LIU *et al.* [22] discovered that for AZ91 magnesium alloys, an increase in coating thickness corresponds with a rise in voltage in the range of 300 to 450 V. However, cracks begin to appear at 450V. SONG and WAN [23] noted that in silicate electrolytes, the optimal corrosion resistance is achieved with a coating prepared at 350 V due to its minimal porosity. YAO *et al.* [24], through XRD analysis, confirmed that a higher voltage fosters the formation of the MgO phase, thereby enhancing the hardness of the coating. Furthermore, the evolution of composite coating technology offers innovative perspectives for boosting MAO performance. For example, LIU *et al.* [25] significantly improved the corrosion resistance of WE43 magnesium alloy by integrating layer-by-layer self-assembly technology with MAO. SHANG *et al.* [26] incorporated MAO with graphene oxide (GO), leveraging the physical barrier effect of GO to further seal the coating pores.

Despite the existing research, a systematic study exploring the relationship between coating structure evolution and corrosion resistance of AZ31B magnesium alloy across a broad voltage range (300–450V) remains insufficient. Recent studies indicate that factors such as surface roughness [27], electrolyte type [28], and post-treatment modification [29, 30] interact with voltage, influencing the coating performance. These variables should be incorporated into the mechanistic analysis.

The relationship between the current density and the voltage in the MAO process is determined by the electrical mode. In this study, the constant voltage mode was adopted. In this mode, the applied voltage directly determines the electric field strength and the plasma discharge intensity, which are the main factors for coating growth rate and microstructure. Therefore, although current density affects the reaction kinetics to some extent, it is the applied voltage that determines the energy input of the whole process and the final characteristics of the coating.

Therefore, this work aims to systematically elucidate the influence of termination voltage (300–450 V) on the MAO coating for AZ31B alloy within a specific silicate electrolyte system and a fixed processing time. The findings are expected to provide a fundamental understanding for refining the MAO process under these specific conditions.

## 2. EXPERIMENTAL METHODS

### 2.1. Substrate pretreatment and experimental materials

The experiment employs AZ31B magnesium alloy as the foundational material, characterized by the following chemical composition (wt.%): Aluminum (Al) ranging from 2.5 to 3.5, Zinc (Zn) from 0.6 to 1.4, Manganese (Mn) between 0.2 and 1.0, Silicon (Si) at a maximum of 0.08, Calcium (Ca) not exceeding 0.04, Copper (Cu) capped at 0.01, Iron (Fe) limited to 0.003, Nickel (Ni) up to 0.001, with the remainder being Magnesium (Mg). The alloy is precision-cut into samples measuring 30 mm × 20 mm × 2 mm and meticulously polished in a methodical sequence utilizing 800#, 1000# and 1200# SiC sandpaper until a smooth, flat surface is achieved, ensuring the removal of the oxide layer and any machining marks. Subsequent to the polishing process, the samples undergo an ultrasonic cleaning in anhydrous ethanol for a duration of 10 minutes to eliminate surface impurities, after which they are appropriately dried and set aside for subsequent use.

The electrolyte utilized in this study is based on a silicate system, characterized by the following composition: 7 g/L NaF, 10 g/L NaOH, 5 g/L $Na_2SiO_3$, 4 g/L $Na_2B_4O_7$, 4 mL/L $C_3H_8O_3$, and 4 mL/L $C_6H_{15}NO_3$. All chemicals employed were sourced from Tianjin Damao Chemical Reagent Factory (China). This specific formulation facilitates the generation and densification of ceramic phases during the micro-arc oxidation process by modulating ion concentration and conductivity.

### 2.2. Micro-arc oxidation process

In the micro-arc oxidation experiment, a bipolar system is employed, utilizing the AZ31B sample as the anode and a stainless-steel plate as the cathode, both submerged in an electrolyte. The experimental setup establishes four distinct voltage parameter groups: 300 V, 350 V, 400 V, and 450 V, while maintaining other process parameters

constant, such as a frequency of 500 Hz, a current of 1.5 A, and a processing duration of 15 minutes. The voltage was applied using a linear ramp-up method at a controlled rate of 30 V/min from the initiation voltage (0 V) until reaching the target final voltage (300, 350, 400, or 450 V). This controlled increase prevents instantaneous high-current breakdown, which can lead to coarse microstructures and defects such as microcracks. Throughout the oxidation process, the voltage exerts a direct influence on the discharge energy density and the intensity of the plasma reaction. At a lower voltage (300 V), the discharge remains in the spark stage, resulting in a sluggish growth of the coating; upon elevation of the voltage to 350 V, the plasma energy becomes adequate to melt the oxides, thereby forming dense phases of MgO and magnesium silicate; however, when the voltage escalates to 450 V, the intensity of the discharge might induce microcracks on the coating surface.

### 2.3. Coating characterization methods

The surface morphology and elemental composition of the coatings were characterized using a scanning electron microscope (SEM, Quanta 450 FEG, USA) and an energy dispersive spectrometer (EDS). Cross-section samples were embedded in epoxy resin, polished, and subsequently used to observe the thickness of the coating and its interfacial bonding state with the matrix. The phase composition of the MAO coatings was detected using an X-ray diffractometer (XRD, cmAX-RC, Japan), and the resulting XRD patterns were analyzed with JADE 9. The presence and relative content of crystalline phases such as MgO and $Mg_2SiO_4$ were determined by comparing them with standard cards (JCPDS). Porosity was calculated using image processing technology. The three-dimensional morphology of the surface of the MAO coating and its roughness was obtained using a 3D imaging system attached to an optical microscope (OM, Olympus DSX510, Japan). Electrochemical tests were conducted using a traditional tripartite electrode system. This system consisted of a saturated calomel reference electrode, a platinum auxiliary electrode with dimensions of 10 mm x 10 mm, and a sample of the same dimensions used as the working electrode. The corrosion resistance of the coating was evaluated through potentiodynamic polarization curves (PPC) and electrochemical impedance spectroscopy (EIS) using an electrochemical workstation (Corrtest CS2350M, China). Prior to both tests, the open circuit potential (OCP) of the samples was measured, with a test duration of six hundred seconds. The PPC measurement range was set from –1.1 V to –1.8 V, while the EIS measurement range spanned from 0.1 Hz to 100,000 Hz. A specified solution was utilized for all electrochemical testing. For each parameter, three samples were tested. Contact Angle Measurement: The contact angle measurement was performed using a specialized instrument (PERFECT WAM100, China). Deionized water droplets, each with a volume of 5 μL, were placed on the coated surface, and the contact angle was measured at five different points on each specimen. The average value of these measurements was then used to assess surface wettability. The Vickers hardness of the surface was determined using a Vickers hardness meter (HVS-1000). Under a load of 100 g and a holding time of 10 seconds, five points on the surface were tested for each voltage condition to mitigate edge effects. This load was selected to obtain a comparative evaluation of the coating's mechanical resistance while minimizing substrate influence for the majority of the coatings.

## 3. RESULTS AND DISCUSSION

### 3.1. Voltage dependence of the coating morphology

The Surface morphology of coatings and distribution of silicon elements in the MAO coating at varying voltages is depicted in Figure 1. EDS elemental mapping was further conducted to examine the distribution of constituent elements. When a high-voltage electric field is applied to the metal surface, the intense heat and pressure produced by arc discharge initiate plasma chemical reactions between the metal substrate and the electrolyte. This results in the formation of a ceramic oxide film that is metallurgically bonded to the substrate. The changes in surface morphology of the AZ31B magnesium alloy's micro-arc oxidation coating at different voltages provide insights into how plasma discharge intensity regulates coating growth. At a lower voltage setting of 300 V (Figure 1a), the coating surface exhibits numerous irregular pores with diameters ranging from 1 to 3 μm, rough pore edges, and an uneven accumulation of molten oxides. This is attributed to the subdued plasma reaction from the low-energy discharge, leading to minimal molten material expulsion and rapid cooling, which results in an incompletely sealed discharge channel [31]. As the voltage increases to 350 V (Figure 1b), the distribution of pores becomes uniform, their edges smoother, and molten oxides accumulate more densely, forming a flat, uniform surface structure. This suggests that the discharge of energy at medium voltage levels is adequate to encourage complete melting and even spreading of oxides, thereby enhancing the surface flatness of the coating. At 400 V (Figure 1c), a few larger pores, with diameters of 2~4 μm, emerge on the surface. With the increase of final voltage, the pore size becomes larger [30]. Some adjacent pores amalgamate due to the intense discharge-induced ejection of molten material, creating a polygonal contour pore structure. Even though the discharge energy is further amplified, local overheating increases the fluidity of the molten oxide

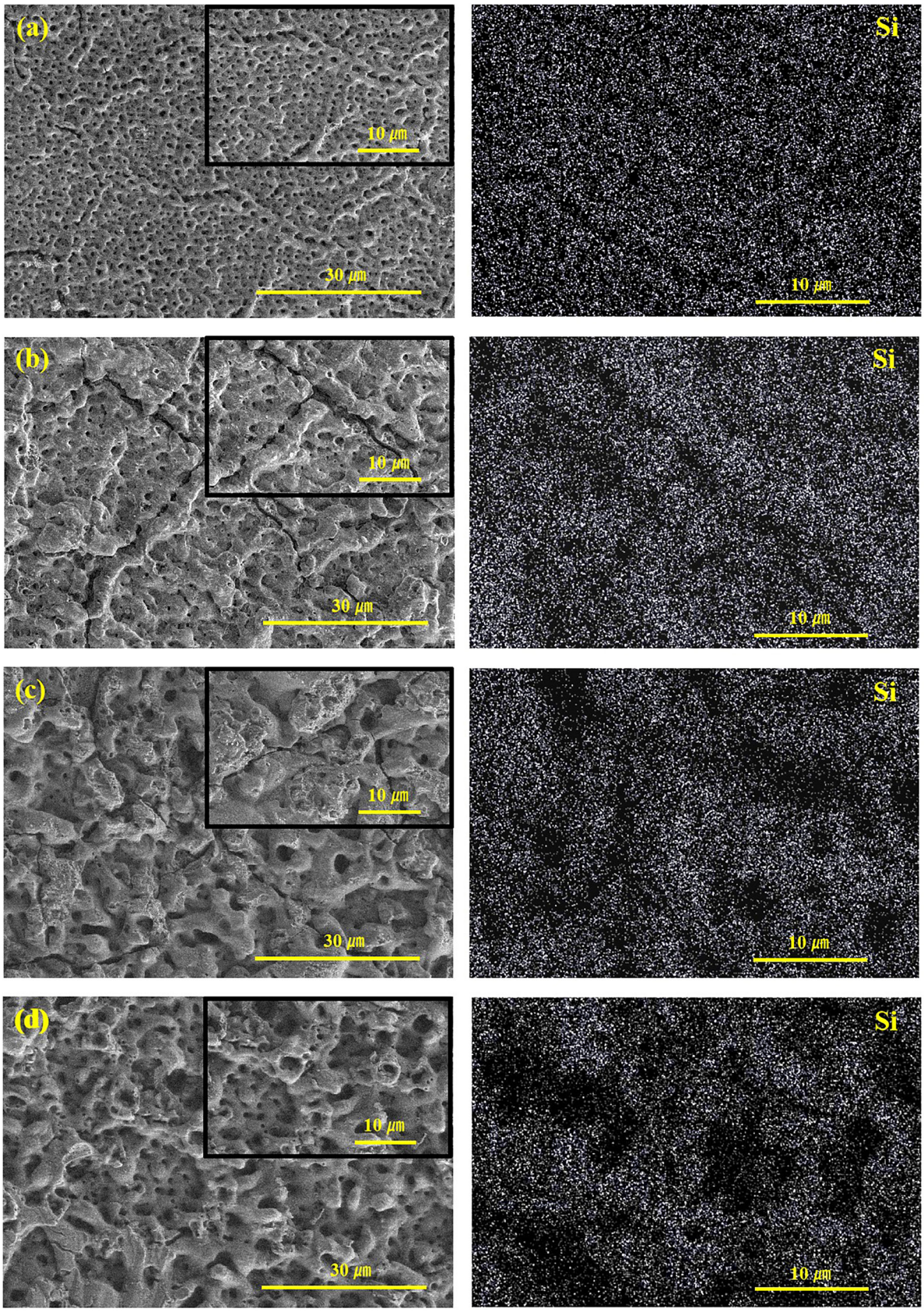


**Figure 1:** Surface morphology of coatings and distribution of silicon elements in the MAO coating with different voltages. (a) 300 V, (b) 350 V, (c) 400 V, (d) 450 V.

state, leading to pore fusion. Under the high voltage of 450 V (Figure 1d), distinct net-like cracks appear on the coarse surface, with a crack width of approximately 1~5 μm [32]. To a certain degree, when the voltage applied surpasses a critical threshold, the coating ceases to optimize and instead becomes prone to peeling and roughness [21]. JIANG *et al.* [33] illustrated that high voltage in an electrolyte triggers intense spark arcing, which leads to adverse effects such as thermal cracking of the coating. This is attributed to the instantaneous hot temperatures caused by excessive discharge of energy, which leads to a concentration of thermal stress inside the coating. This exceeds the tensile strength of the ceramic layer, causing it to crack. Voltage regulates the energy density of plasma discharge, influencing the ejection number of molten oxides, cooling rate, and thermal stress distribution. Consequently, it determines the pore size, distribution uniformity, and crack initiation behavior of the coating surface.

The cross-sectional SEM analysis of the micro-arc oxidation coating on the AZ31B magnesium alloy at varying voltages (Figure 2) demonstrates the dynamic coupling mechanism of coating growth with voltage. At a low voltage of 300 V (Figure 2a), the coating thickness is only 5–8 μm, with an insufficient proportion of dense layer, a blurred boundary between the inner layer and substrate, and numerous penetrating channels. This is attributed to the slow deposition rate of oxides due to low-energy discharge, resulting in a porous structure after the melt cools. At 350 V (Figure 2b), the coating thickness increases to 10–15 μm, with a higher proportion of dense layer and the inner layer forming an interlocking metallurgical bond with the substrate. The EDS surface scan reveals a uniform distribution of the O element, suggesting that the plasma discharge energy at medium voltage is adequate to facilitate the full reaction of $Mg^{2+}$ with $O^{2-}$ to form MgO, and to form a composite structure

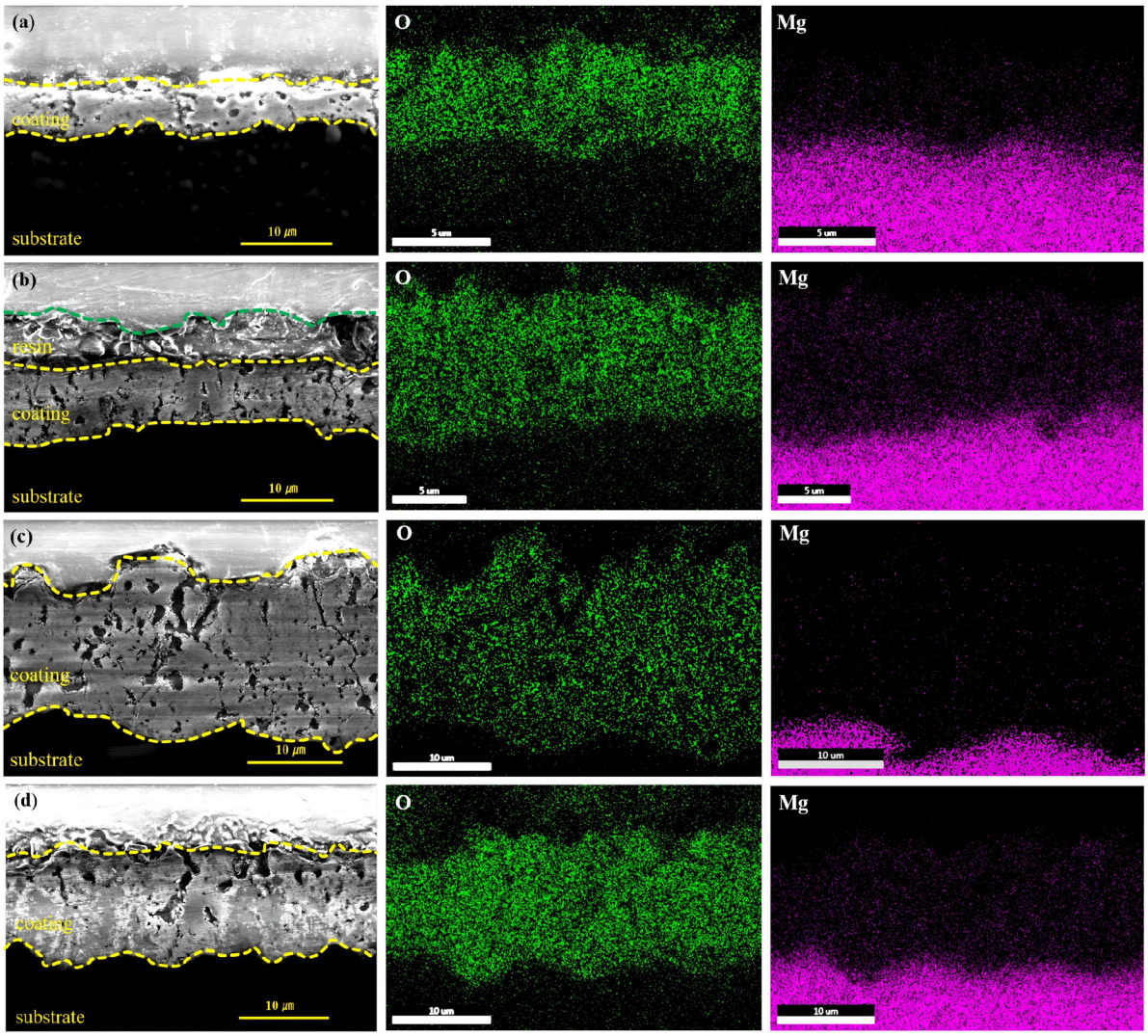


**Figure 2:** Cross-sectional SEM micrographs and elemental distribution of the MAO coating at different voltages. (a) 300 V; (b) 350 V; (c) 400 V; (d) 450 V.

with the silicate phase. At 400 V (Figure 2c), the coating thickness reaches its maximum value of 22–25 μm, with an increased proportion of dense layer and the Mg and O elements forming a solid solution transition zone at the interface, which enhances the bonding force between the coating and the substrate, confirming the trend of high voltage promoting the formation of MgO phase [34]. At a high voltage of 450 V (Figure 2d), the coating thickness decreases to 18–20 μm, with penetrating cracks appearing in the cross-section and the dense layer structure being destroyed. The nonlinear relationship between the thickness evolution law and the discharge energy indicates that: at the beginning of the voltage increase, the increase in plasma discharge energy promotes the deposition of oxides, and the thickness grows linearly; however, at 450 V, the instantaneous high temperature generated by the intense discharge causes local melting and splashing of the coating, which reduces the effective thickness. Furthermore, EDS elemental mapping was performed to analyze the composition distribution. As shown in Figure 1, the Si element is uniformly distributed across the coating surface, indicating the successful incorporation of silicate species from the electrolyte into the coating matrix during the MAO process. This provides fundamental evidence for the formation of silicate-containing phases in the coating.

### 3.2. Composition and phase analysis

Figure 3 presents XRD patterns of MAO coatings fabricated on AZ31B magnesium alloy under different termination voltages. Phase identification confirms that the coatings are primarily composed of crystalline MgO and forsterite ($Mg_2SiO_4$). The identification of $Mg_2SiO_4$ phase is based on its characteristic diffraction peaks at approximately 36.8°, 48.4°, and 54.9°, which perfectly match the standard pattern of forsterite (JCPDS #00-034-0556), as shown in Figure 3. This phase identification result aligns with numerous studies on MAO of magnesium alloys in silicate electrolyte systems [35–37] and mutually corroborates with the uniform distribution of silicon element within the coating revealed by EDS mapping (Figure. 1).

The formation mechanism of MgO resembles conventional anodization, involving outward migration of $Mg^{2+}$ from the substrate and inward migration of $O^{2-}$/$OH^-$ from the electrolyte, followed by their combination. In contrast, the presence of $Mg_2SiO_4$ represents a hallmark feature of MAO processes in silicate systems, originating from active participation of silicate ions from the electrolyte during plasma chemical reactions. Under the instantaneous high-temperature and high-pressure conditions generated by micro-arc discharges, silicate ions in the electrolyte undergo hydrolysis and dehydration to form reactive $SiO_2$ [21]. Simultaneously, the extreme temperatures produced during discharge events are sufficient to instantaneously melt both the pre-existing MgO layer on the substrate surface and the newly formed $SiO_2$. When the micro-arc extinguishes, the molten mixture undergoes rapid cooling due to contact with the electrolyte, triggering high-temperature phase transformation where $SiO_2$ reacts with MgO to ultimately form thermodynamically stable forsterite ($Mg_2SiO_4$) [36].

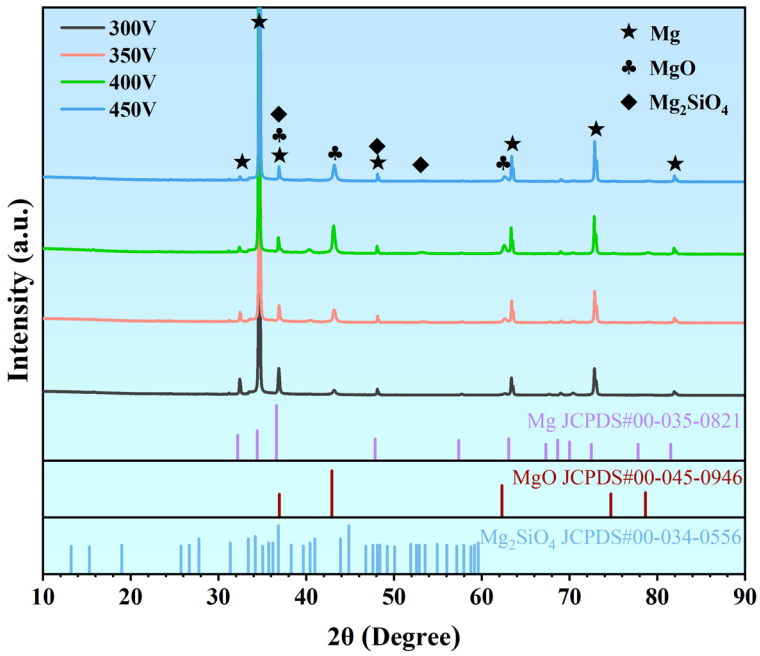


**Figure 3:** XRD patterns of the MAO coating in comparison with standard diffraction peaks for Mg (JCPDS #00-035-0821), MgO (JCPDS #00-045-0946), and forsterite (Mg2SiO4, JCPDS #00-034-0556).

As the voltage increases from 300 V to 450 V, the intensity of MgO diffraction peaks significantly, consistent with literature reports indicating that higher voltages promote MgO formation [21, 34]. This phenomenon correlates with EDS results, suggesting that elevated voltages and intensified discharge environments not only enhance plasma discharge energy to facilitate direct combination of $Mg^{2+}$ and $O^{2-}$, but also potentially influence cooling rates of molten oxides and phase transformation kinetics through increased thermal input, collectively resulting in increased relative content of MgO in the coatings.

### 3.3. Mechanical and surface properties

Figure 4 illustrates the variation curves of coating contact angle, hardness, and roughness. The surface roughness average (Ra) demonstrates a non-linear trend of initially increasing before subsequently decreasing as voltage rises, creating a synergistic correlation with the development patterns of both contact angle and hardness. At 300 V, the coating's roughness measures 1.869 μm, corresponding to a surface characterized by numerous irregular pores. This is due to the weak discharge intensity under low voltage which results in uneven accumulation of molten oxides, forming a porous, rough structure. As the voltage increases to 350 V, the roughness escalates to 2.126 μm (Figure 4d). This was because the MAO reaction became more intense as the voltage increased [21]. The improvement in discharge uniformity at this stage results in decreased pore size, denser distribution, and intensified surface micro-undulation. This "uniform porous" structure lowers the contact angle to 2.21° via enhancement of the capillary effect. Concurrently, the increase in roughness and densification of the coating collectively elevate the hardness to 305.75 HV.

At 400 V, there is a marginal decrease in roughness to 2.125 μm (Figure 4e). Despite a slight increase in porosity due to intensified discharge, the surface morphology trends towards regularity, and the merging of large-diameter pores leads to a reduction in micro-undulations. The significant increase in the MgO phase at this stage, with its highly polar surface dominating the wettability, results in a further decrease in the contact angle to 1.59°. The synergistic effect of the dense structure and high hardness phase (MgO) propels the hardness to its peak value of 329.19 HV. Finally, at 450 V, the roughness dramatically decreases to 2.054 μm (Figure 4f). The emergence of penetrating cracks on the surface leads to stress concentration, subsequently causing a reduction in hardness to 254 HV [23]. Violent discharge disrupts the uniformity of the coating. While this loose structure reduces surface roughness, it also causes the contact angle to increase significantly to 19.48°. The roughness initially increases and then decreases as the voltage rises, mirroring the trend of porosity changes.

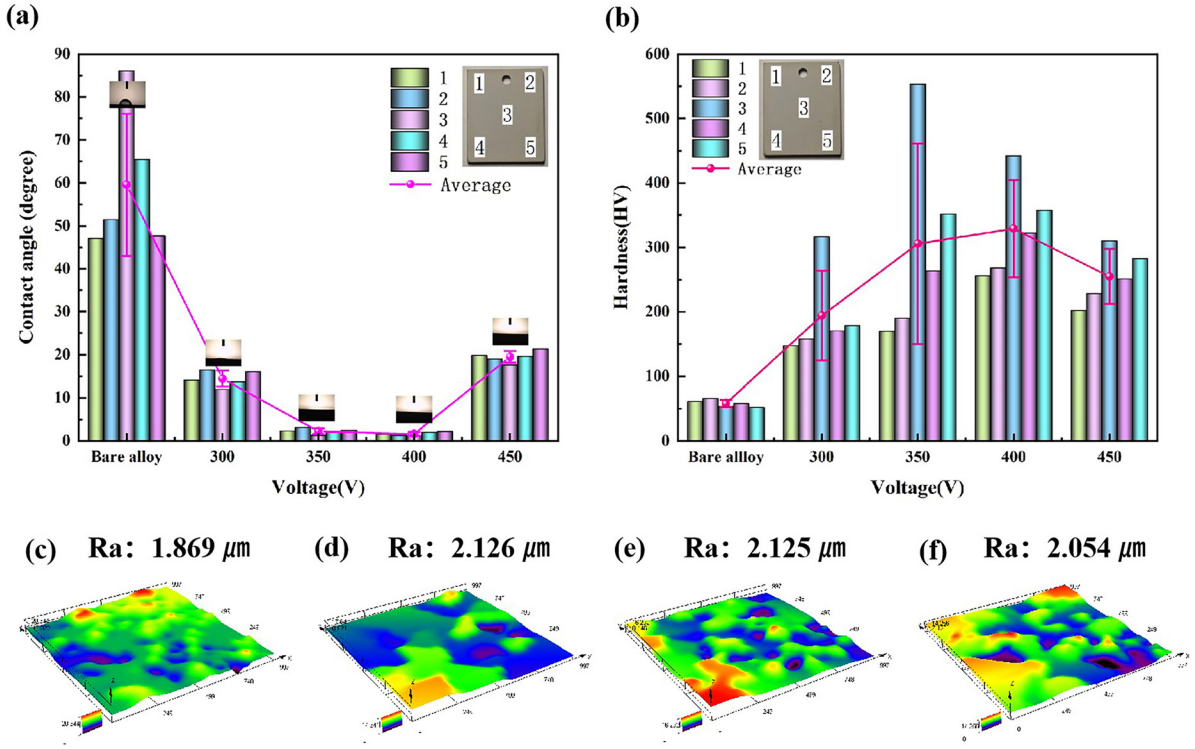


**Figure 4:** Contact angles, microhardness and roughness of AZ31B magnesium alloy substrate and MAO coatings with different voltages. (a) Contact angles; (b) Microhardness; (c) 300 V; (d) 350 V; (e)400 V; (f) 450 V.

The Vickers microhardness values reported in Figure 4b are derived from indentations with typical diagonal lengths ranging from 20 to 40 μm. Surface morphology of these indentations (provided in Figure S1) confirmed well-defined impressions without radial cracking, indicating good coating cohesion during testing. It is noteworthy that for the 300 V coating, its lower thickness (5–8 μm) means the indentation depth could be influenced by the softer magnesium substrate, potentially resulting in a slight underestimation of the coating's intrinsic hardness. For the thicker coatings (≥10 μm), this substrate effect is considered negligible, and the values are representative of the coating properties.

In conclusion, a closely interrelated relationship exists between the evolution of roughness and the micro-morphology and phase composition of the coating. At voltages ranging from 350 to 400 V, a balance is achieved between roughness and compactness, thereby optimizing the surface hydrophilicity and mechanical properties of the coating. The observed decrease in roughness at 450 V is essentially a macroscopic manifestation of the coating structure undergoing deterioration. This observation corroborates the mechanism that a moderate voltage (350V–400V) enhances comprehensive performance by simultaneously regulating surface texture and phase composition.

### 3.4. Corrosion resistance analysis

The evolution of coating properties reveals a critical trade-off governed by voltage. While the coatings prepared at 400 V exhibit greater thickness and a higher content of the hard MgO phase-leading to peak microhardness-this comes at a cost to their corrosion resistance. The intense plasma discharge at these higher voltages generates excessive thermal stress and leads to the coalescence of molten oxides, resulting in the formation of larger, interconnected pores and micro-cracks (as seen in Figure 1c). These structural defects become the dominant factor in determining the coating's long-term performance, as they provide low-resistance pathways for the corrosive medium to penetrate the coating and reach the underlying substrate. Therefore, we analysis its Corrosion resistance.

The potentiodynamic polarization curves for both the AZ31B magnesium alloy substrate and the MAO coatings, post-exposure to varying voltages in a 3.5 wt.% NaCl solution, are depicted in Figure 5. The corrosion potential ($E_{corr}$) and corrosion current density ($I_{corr}$) were determined using the Tafel extrapolation method to assess the corrosion resistance of the MAO coatings. In this context, $E_{corr}$ is inversely related to the corrosion tendency, suggesting the likelihood of corrosion occurrence. Meanwhile, $I_{corr}$ correlates with the corrosion rate; a reduced $I_{corr}$ signifies a slower corrosion rate, pointing to superior anti-corrosion performance [38]. Thus, a high corrosion potential and a low corrosion current density indicate the robust corrosion resistance of MAO coatings. As evidenced from Table 1, the $E_{corr}$ for the MAO coatings surpassed that of the substrate, while the $I_{corr}$ showed the opposite trend, highlighting the enhanced corrosion resistance of the substrate by the MAO

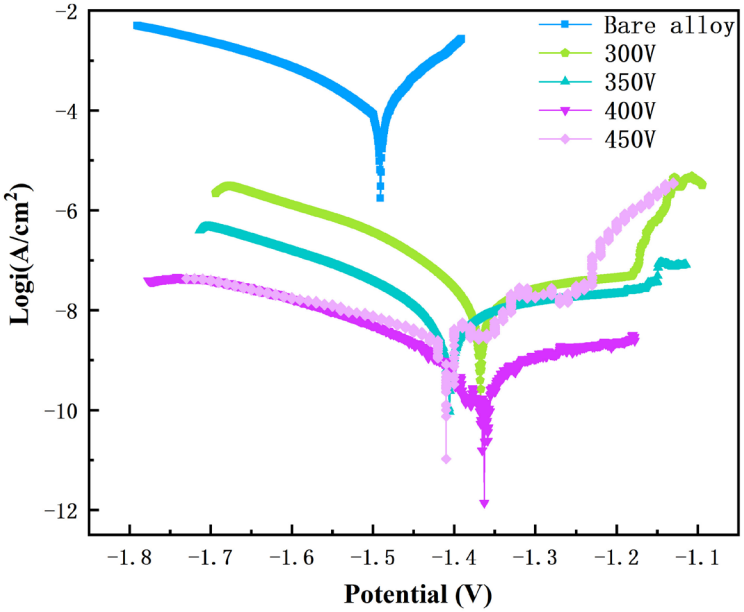


**Figure 5:** Dynamic potential polarization curves of AZ31B magnesium alloy substrate and MAO coatings with different voltages.

coatings. From Figure 5 and Table 1, it is evident that initially, when the voltage fluctuates between 300–350 V, both the corrosion potential and current density decrease as the applied voltage increases, suggesting the formation of a denser coating. However, when the voltage escalates from 400 to 450 V, despite the substantial coating thickness, the corrosion potential decreases while the corrosion current density elevates due to cracking and penetration. The most negative corrosion potential of –1.4060 V and the minimum corrosion current density of $1.5734 \times 10^{-8}$ A/cm$^2$ are observed at an applied voltage of 350 V. These values indicate that the 350 V coating exhibits the slowest corrosion kinetics and superior corrosion resistance. Nevertheless, a significant increase in the corrosion rate is noted due to the presence of cracks at 450 V [16].

EIS analysis, as shown in Figure 6, reveals that voltage significantly influences the corrosion resistance of the MAO coating on AZ31B magnesium alloy. The Nyquist plots for the MAO coatings are presented in Figure 6(a). All MAO coatings display capacitive reactance curves in the high-frequency region. As the capacitive circuit radius increases, the corrosion rate decreases [21]. Notably, the capacitive loop radius of the MAO

**Table 1:** Electrochemical test parameters of AZ31B magnesium alloy substrate and MAO coating with different voltages.

| SAMPLE | $E_{corr}$/V | $I_{corr}$ / (A•cm$^{-2}$) |
|---|---|---|
| Bare alloy | –1.4907 | $1.6824 \times 10^{-4}$ |
| 300V | –1.3675 | $3.4145 \times 10^{-8}$ |
| 350V | –1.4060 | $1.5734 \times 10^{-8}$ |
| 400V | –1.3629 | $5.4556 \times 10^{-6}$ |
| 450V | –1.4068 | $5.5280 \times 10^{-5}$ |

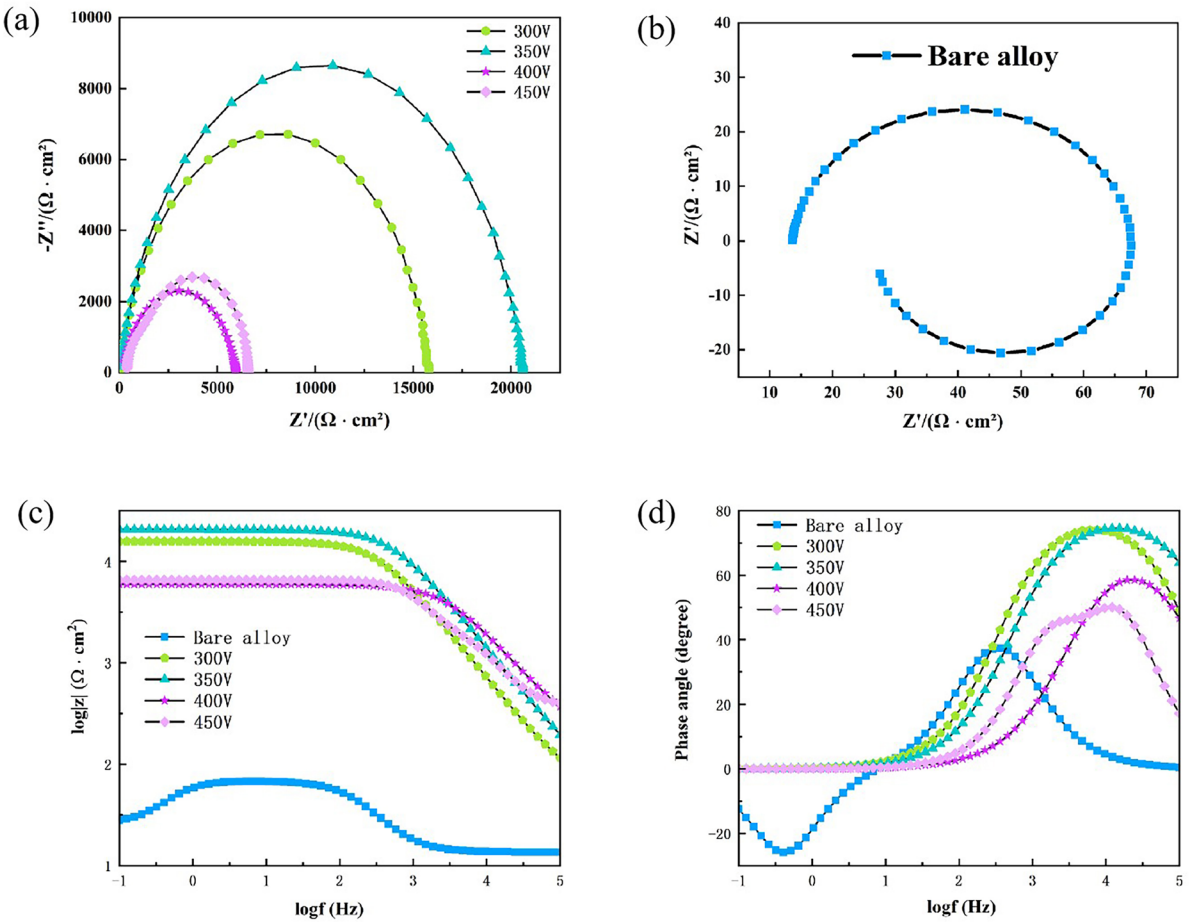


**Figure 6:** Electrochemical impedance spectra of AZ31B magnesium alloy substrate and MAO coated at 300 V, 350 V, 400 V and 450 V immersed in 3.5wt.% NaCl solution. (a) Nyquist plots (coating); (b) Nyquist plots (substrate); (c) Porter modulus plots; (d) Porter phase plots.

coating is significantly larger than that of the substrate. An EIS test conducted in a 3.5 wt.% NaCl solution demonstrated that the MAO coating at 350V exhibited optimal corrosion resistance. This was evidenced by its Nyquist diagram, which displayed the largest capacitive arc and a low-frequency ($10^{-1}$ Hz) impedance modulus reaching $10^4$ Ω·cm$^2$. This corresponds to a charge transfer resistance ($R_p$) of 7.407 × $10^3$ Ω·cm$^2$, suggesting substantial charge transfer resistance and reduced electrolyte penetration. The interface resistance (Rb) measured 15.610 × $10^3$ Ω·cm$^2$, markedly higher than other voltage groups (Table 2, 3). The "$R_s$-($Q_p$-$R_p$) -($Q_b$-$R_b$)" was selected as the equivalent circuit model for the MAO coatings [39, 40], as shown in (Figure 7b), where the constant phase element $Q_p$ had an exponent $n_p$ = 0.923, indicating a structure consistent with an ideal capacitor and suggesting a uniform, dense coating. The equivalent electrical circuits (EECs) employed for data fitting, as depicted in Figure 7, were selected based on their physical correspondence to the electrode system and their ability to provide an excellent fit for the experimental data. The model for the bare alloy (Figure 7a) accounts

**Table 2:** EIS fitting data for AZ31B magnesium alloy substrate.

| Sample | $R_s$ (Ω·cm$^2$) | $Q_1$ (Ω$^{-1}$·s$^n$·cm$^{-2}$) | $n_1$ | $R_1$ (Ω·cm$^2$) | L (Ω$^{-1}$·s$^n$·cm$^{-2}$) | $R_L$ (Ω·cm$^2$) |
|---|---|---|---|---|---|---|
| Bare alloy | 13.580 | 3.437 × $10^{-5}$ | 0.923 | 54.520 | 16.950 | 17.060 |

**Table 3:** EIS fitting data for MAO coatings with different voltages.

| SAMPLE | $R_s$ (Ω·cm$^2$) | $Q_p$ (Ω$^{-1}$·s$^n$·cm$^{-2}$) | $n_p$ | $R_p$ (Ω·cm$^2$) | $Q_b$ (Ω$^{-1}$·s$^n$·cm$^{-2}$) | $n_b$ | $R_b$ (Ω·cm$^2$) |
|---|---|---|---|---|---|---|---|
| 300V | 51.960 | 2.292 × $10^{-8}$ | 0.972 | 1.310 × $10^3$ | 1.765 × $10^{-8}$ | 0.984 | 16.910 × $10^3$ |
| 350V | 59.610 | 2.268 × $10^{-8}$ | 0.923 | 7.407 × $10^3$ | 0.803 × $10^{-8}$ | 1.000 | 15.610 × $10^3$ |
| 400V | 54.550 | 4.170 × $10^{-8}$ | 0.829 | 2.911 × $10^3$ | 1.306 × $10^{-8}$ | 0.965 | 5.658 × $10^3$ |
| 450V | 57.510 | 5.420 × $10^{-8}$ | 0.866 | 2.922 × $10^3$ | 4.393 × $10^{-8}$ | 0.945 | 4.364 × $10^3$ |

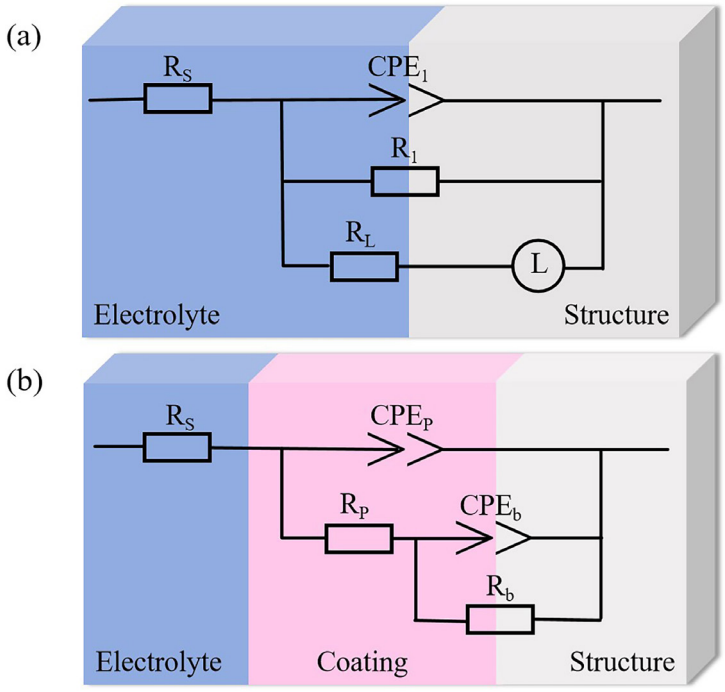


**Figure 7:** Equivalent electrical circuit diagram in 3.5wt.% NaCl solution. (a) AZ31B magnesium alloy matrix; (b) MAO coating.

for the charge transfer resistance ($R_1$) and the double-layer capacitance ($CPE_1$), with an additional inductive loop (L, $R_L$) to describe the relaxation of adsorbed intermediates during magnesium dissolution. For the MAO coatings, the two-time-constant model $R_s$-($Q_p$-$R_p$) -($Q_b$-$R_b$) (Figure 7b) was adopted to represent the duplex-layer structure of the coating, which consists of a porous outer layer (described by $Q_p$-$R_p$) and a dense inner barrier layer (described by $Q_b$-$R_b$). This model is well-established for MAO coatings and is consistent with the cross-sectional morphology observed in Figure 2.

The presence of the low-frequency inductive loop for the bare AZ31B substrate, a characteristic feature of actively corroding magnesium alloys, is incorporated into its EEC. This inductive behavior is widely attributed to the relaxation process of intermediately adsorbed species (e.g., $Mg^+$) on the metal surface or to the initiation and repassivation of metastable pitting sites within the chloride-containing solution.

Conversely, at 450 V, Rp decreased to $2.922 \times 10^3$ Ω·cm$^2$, and the $Q_p$ exponent $n_p = 0.866$, indicative of coating non-uniformity due to through-cracks. Although the 400 V and 450 V coating is thicker and possesses a higher MgO content, its corrosion resistance is inferior to that of the 350 V coating. This can be mechanistically attributed to the coarsened pore structure and the initiation of micro-cracks, which compromise the coating's barrier effectiveness. The beneficial barrier property of the dense MgO phase is thus offset by the presence of these macroscopic defects, which facilitate rapid electrolyte penetration. This underscores that for corrosion protection, the compactness and structural integrity of the coating are more critical than mere thickness or hardness.

The Bode plot illustrates that the phase angle of the 350 V coating remains consistently above 60° across a broad frequency range, attesting to its effective barrier against $Cl^-$ penetration. This, when combined with the dense layer observed in SEM analyses-which constitutes 50% of the coating-and the synergistic effect of MgO and $Mg_2SiO_4$ phases as confirmed by XRD, suggests that a moderate voltage (350V) bolsters corrosion resistance by optimizing coating density, phase composition, and interface binding force. Conversely, an excessively high voltage (450V) precipitates cracks owing to thermal stress, resulting in a notable reduction in impedance and a concomitant decline in corrosion resistance. This finding aligns with the conclusion drawn from the potentiodynamic polarization curve, which identifies the 350V coating as having the lowest corrosion current density ($1.5734 \times 10^{-8}$ A·cm$^{-2}$), thereby affirming a clear structure-effect relationship between the impedance characteristics of the MAO coating and its microstructural evolution. In summary, all MAO coatings exhibit enhanced corrosion resistance compared to bare alloys, as evidenced by all parameters.

## 4. CONCLUSIONS

This study presents a systematic investigation into the fabrication of magnesium alloy MAO coatings by controlling the termination voltage. The findings provide both experimental evidence for optimizing surface protection processes for magnesium alloys and clear guidance for industrial applications. Drawing from the experimental results and subsequent discussions presented herein within the constraints of the applied silicate electrolyte, 500 Hz, and 15-minute processing time, we deduce the following conclusions:

- The voltage significantly influences the structure of the coating. At 300 V, the coating exhibits porosity, achieving its lowest porosity and optimal density at 350V. The thickness peaks at 400 V, while cracks emerge at 450V due to thermal stress.
- Phase and Performance Correlation. The coating comprises MgO and $Mg_2SiO_4$. An increase in voltage encourages the formation of MgO. The hardness of the coating reaches its maximum at 400V, which corresponds to the lowest contact angle, suggesting optimal hydrophilicity.
- Corrosion Resistance Control Mechanism. The coating subjected to 350V exhibits the lowest corrosion current density and the highest impedance modulus, signifying optimal corrosion resistance. This outcome is attributed to the concurrent formation of a dense structure and phase, yielding composite protection. Nevertheless, excessive voltage can result in performance degradation. This work provides a systematic dataset and a clear mechanistic understanding that serves as a valuable foundation for the optimization of MAO processes for magnesium alloys.

## 5. ACKNOWLEDGMENTS

We would like to appreciate the Sector Foundation Project (2023-JCJQ-JJ-0958), the Beijing Municipal Natural Science Foundation (No. 3232016), the National Natural Science Foundation of China (Nos. 52105236 and 52130509), the Scientific research projects in higher education institutions of Hebei province (Grant Number QN2022039) and FBV INC for funding support.

## 6. BIBLIOGRAPHY


[1] MORDIKE, B.L., EBERT, T., "Magnesium - properties - applications - potential", *Materials Science and Engineering A*, v. 302, n. 1, pp. 37–45, 2001. doi: http://doi.org/10.1016/S0921-5093(00)01351-4.

[2] POLLOCK, T.M., "Weight loss with magnesium alloys", *Science*, v. 328, n. 5981, pp. 986–987, 2010. doi: http://doi.org/10.1126/science.1182848. PMid:20489013.

[3] ZHANG, Z., ZHANG, J., WANG, W., *et al*., "Unveiling the deformation mechanism of highly deformable magnesium alloy with heterogeneous grains", *Scripta Materialia*, v. 221, pp. 114963, 2022. doi: http://doi.org/10.1016/j.scriptamat.2022.114963.

[4] PAWAR, S., SLATER, T.J.A., BURNETT, T.L., *et al*., "Crystallographic effects on the corrosion of twin roll cast AZ31 Mg alloy sheet", *Acta Materialia*, v. 133, pp. 90–99, 2017. doi: http://doi.org/10.1016/j.actamat.2017.05.027.

[5] UMOREN, S.A., SOLOMON, M.M., MADHANKUMAR, A., *et al*., "Exploration of natural polymers for use as green corrosion inhibitors for AZ31 magnesium alloy in saline environment", *Carbohydrate Polymers*, v. 230, pp. 115466, 2020. doi: http://doi.org/10.1016/j.carbpol.2019.115466. PubMed PMID: 31887965.

[6] LI, Y., LI, H., XIONG, Q.M., *et al*., "Multipurpose surface functionalization on AZ31 magnesium alloys by atomic layer deposition: tailoring the corrosion resistance and electrical performance", *Nanoscale*, v. 9, n. 25, pp. 8591–8599, 2017. doi: http://doi.org/10.1039/C7NR00127D. PMid:28475194.

[7] TORÓS, P., FONTINOVO GOYENECHEA, F., GILABERT, U., *et al*., "Obtención y caracterización de recubrimientos de biovidrio sobre la aleación de Mg AZ31", *Revista Matéria*, v. 23, n. 2, pp. e-12048, 2018. doi: https://doi.org/10.1590/S1517-707620180002.0384.

[8] SINGH, P.K., LOGESH, K., SURESH KUMAR, S., *et al*., "Revolutionizing the material performance of AZ64/$ZrB_2$ composites for engineering applications", *Revista Matéria*, v. 30, pp. e20240356, 2025. doi: https://doi.org/10.1590/1517-7076-RMAT-2024-0356.

[9] YIN, J., CHEN, Z., DAI, X., *et al*., "Microstructure and mechanical properties of laser welded joint of cerium-containing magnesium alloy", *Materials Research*, v. 27, pp. e20240022, 2024. doi: https://doi.org/10.1590/1980-5373-MR-2024-0022.

[10] CHEN, H., GAO, Q.Y., YE, S., *et al*., "Laser butt welding of thin AZ31B magnesium alloy sheets with and without beam oscillation", *Materials Research*, v. 28, pp. e20250368, 2025. doi: https://doi.org/10.1590/1980-5373-MR-2025-0368.

[11] WAN, H., SONG, D., "Corrosion failure process of organic conductive coating on Mg-RE alloy with PEO in the simulated Xisha atmospheric solution", *Materials Chemistry and Physics*, v. 291, pp. 126771, 2022. doi: http://doi.org/10.1016/j.matchemphys.2022.126771.

[12] YIGIT, O., "Structural, chemical and osteogenic properties of GNS reinforced fluorine-doped strontiumapatite coatings on AZ31 Mg alloys for potential biomedical applications", *Surface and Coatings Technology*, v. 451, pp. 129031, 2022. doi: http://doi.org/10.1016/j.surfcoat.2022.129031.

[13] WANG, X., LU, X., JU, P., *et al*., "Influence of ZnO on thermal control property and corrosion resistance of plasma electrolytic oxidation coatings on Mg alloy", *Surface and Coatings Technology*, v. 409, pp. 126905, 2021. doi: http://doi.org/10.1016/j.surfcoat.2021.126905.

[14] XIE, J., ZHANG, J., ZHANG, Z., *et al*., "Corrosion mechanism of Mg alloys involving elongated long - period stacking ordered phase and intragranular lamellar structure", *Journal of Materials Science and Technology*, v. 151, pp. 190–203, 2023. doi: http://doi.org/10.1016/j.jmst.2023.01.005.

[15] HUSSEIN, R.O., NIE, X., NORTHWOOD, D.O., "An investigation of ceramic coating growth mechanisms in plasma electrolytic oxidation (PEO) processing", *Electrochimica Acta*, v. 112, pp. 111–119, 2013. doi: http://doi.org/10.1016/j.electacta.2013.08.137.

[16] QIAO, Y., KONG, D., "Micro arc oxidation coatings on AZ31B magnesium alloy with different voltages: microstructure, tribocorrosion and electrochemical properties", *Metallurgical and Materials Transactions. B, Process Metallurgy and Materials Processing Science*, v. 56, n. 1, pp. 958–975, 2025. doi: http://doi.org/10.1007/s11663-024-03386-7.

[17] LIU, Y., LIU, S., YU, L., *et al*., "Summary on corrosion behavior and micro-arc oxidation for magnesium alloys", *Journal of Chinese Society for Corrosion and Protection*, v. 35, n. 2, pp. 99–105, 2015. doi: http://doi.org/10.11902/1005.4537.2014.047.

[18] SHANG, W., CHEN, B., SHI, X., *et al*., "Electrochemical corrosion behavior of composite MAO/ so-gel coatings on magnesium alloy AZ91D using combined micro-arc oxidation and sol-gel technique", *Journal of Alloys and Compounds*, v. 474, n. 1-2, pp. 541–545, 2009. doi: http://doi.org/10.1016/j.jallcom.2008.06.135.

[19] ZHANG, Y., CHEN, Y., YU, D., *et al*., "Influence of micro - arc oxidation on mechanical properties of magnesium alloy AZ91D", *Journal of Chinese Society for Corrosion and Protection*, v. 30, n. 3, pp. 222–226, 2010.

[20] CHEN, L., ZHAO, R., QI, H., *et al*., "Influence of voltage modes on microstructure and corrosion resistance of micro - arc oxidation coating on magnesium alloy", *Journal of Adhesion Science and Technology*, v. 37, n. 15, pp. 2232–2246, 2023. doi: http://doi.org/10.1080/01694243.2022.2122294.

[21] LU, J., CAO, G., QUAN, G., *et al*., "Effects of voltage on microstructure and corrosion resistance of micro - arc oxidation ceramic coatings formed on KBM10 magnesium alloy", *Journal of Materials Engineering and Performance*, v. 27, n. 1, pp. 147–154, 2018. doi: http://doi.org/10.1007/s11665-017-3088-6.

[22] LIU, Y., YONG, Q., WU, L., *et al*., "Cerium nitrate and stearic acid modified corrosion-resistant micro-arc oxidation coating on magnesium alloy", *Surface and Coatings Technology*, v. 478, pp. 130461, 2024. doi: http://doi.org/10.1016/j.surfcoat.2024.130461.

[23] SONG, D., WAN, H., "Key factor for the corrosion resistance of MAO coating on Mg alloy", *Materials Chemistry and Physics*, v. 305, pp. 127963, 2023. doi: http://doi.org/10.1016/j.matchemphys.2023.127963.

[24] YAO, W., WU, L., WANG, J., *et al*., "Micro-arc oxidation of magnesium alloys: a review", *Journal of Materials Science and Technology*, v. 118, pp. 158–180, 2022. doi: http://doi.org/10.1016/j.jmst.2021.11.053.

[25] LIU, P., PAN, X., YANG, W., *et al*., "Improved anticorrosion of magnesium alloy via layer-by-layer self-assembly technique combined with micro-arc oxidation", *Materials Letters*, v. 75, pp. 118–121, 2012. doi: http://doi.org/10.1016/j.matlet.2012.02.016.

[26] SHANG, W., WU, F., WANG, Y., *et al*., "Corrosion resistance of micro - arc oxidation/graphene oxide composite coatings on magnesium alloys", *ACS Omega*, v. 5, n. 13, pp. 7262–7270, 2020. doi: http://doi.org/10.1021/acsomega.9b04060. PMid:32280867.

[27] NASHRAH, N., KAMIL, M.P., YOON, D.K., *et al*., "Formation mechanism of oxide layer on AZ31 Mg alloy subjected to micro-arc oxidation considering surface roughness", *Applied Surface Science*, v. 497, pp. 143772, 2019. doi: http://doi.org/10.1016/j.apsusc.2019.143772.

[28] RAM KUMAR, V., MUTHUPANDI, V., "Effect of electrolyte in microarc oxidation on providing corrosion resistance to inhomogeneous microstructure in ZM21 magnesium alloy", *Transactions of the Indian Institute of Metals*, v. 72, n. 6, pp. 1617–1620, 2019. doi: http://doi.org/10.1007/s12666-019-01707-y.

[29] CUI, X., LIN, X., LIU, C., *et al*., "Fabrication and corrosion resistance of a hydrophobic micro-arc oxidation coating on AZ31 Mg alloy", *Corrosion Science*, v. 90, pp. 402–412, 2015. doi: http://doi.org/10.1016/j.corsci.2014.10.041.

[30] ZHANG, S., HU, G., ZHANG, R., *et al*., "Effects of electric parameters on corrosion resistance of anodic coatings formed on magnesium alloys", *Transactions of Nonferrous Metals Society of China*, v. 20, pp. s660–s664, 2010. doi: http://doi.org/10.1016/S1003-6326(10)60557-2.g

[31] XU, C., YAN, X., YANG, H., *et al*., "Effect of voltage on the microstructure and corrosion properties of MAO coatings on biodegradable ZK60 Mg alloys", *International Journal of Electrochemical Science*, v. 13, n. 4, pp. 3555–3565, 2018. doi: http://doi.org/10.20964/2018.04.60.

[32] MOEDANO, M., SERDECHNOVA, M., STARYKEVICH, M., *et al*., "Active protective PEO coatings on AA2024: role of voltage on in-situ LDH growth", *Materials & Design*, v. 120, pp. 36-46, 2017. doi: http://doi.org/10.1016/j.matdes.2017.01.097.

[33] JIANG, X., LU, S., TANG, L., *et al*., "Influence of negative voltage on micro-arc oxidation of magnesium alloy under two steps voltage-increasing mode", *Key Engineering Materials*, v. 575-576, pp. 472–476, 2014. doi: https://doi.org/10.4028/www.scientific.net/KEM.575-576.472.

[34] LIU, D., LIU, J., LIU, G., *et al*., "Study on corrosion resistance of LDH/micro-arc oxidation composite superhydrophobic coatings on AZ31 magnesium alloy", *Coatings*, v. 13, n. 3, pp. 643, 2023. doi: http://doi.org/10.3390/coatings13030643.

[35] JIN, S., MA, X., WU, R., *et al*., "Effect of carbonate additive on the microstructure and corrosion resistance of plasma electrolytic oxidation coating on Mg-9Li-3Al alloy", *International Journal of Minerals Metallurgy and Materials*, v. 29, n. 7, pp. 1453–1463, 2022. doi: http://doi.org/10.1007/s12613-021-2377-0.

[36] Guo, H.F., AN, M.Z., HUO, H.B., *et al*., "Microstructure characteristic of ceramic coatings fabricated on magnesium alloys by micro-arc oxidation in alkaline silicate solutions", *Applied Surface Science*, v. 252, n. 22, pp. 7911–7916, 2006. doi: https://doi.org/10.1016/j.apsusc.2005.09.067.

[37] YANG, S., SUN, R., CHEN, K., "Self-healing performance and corrosion resistance of phytic acid/cerium composite coating on microarc-oxidized magnesium alloy", *Chemical Engineering Journal*, v. 428, pp. 131198, 2022. doi: http://doi.org/10.1016/j.cej.2021.131198.

[38] SHI, Z., LIU, M., AURENS, A., "Measurement of the corrosion rate of magnesium alloys using Tafel extrapolation", *Corrosion Science*, v. 52, n. 2, pp. 579–588, 2010. doi: http://doi.org/10.1016/j.corsci.2009.10.016.

[39] LIU, Y., DUAN, J., ZHANG, J., *et al*., "Active corrosion protection of micro - arc oxidation - based composite coating on magnesium alloy: multiple roles of ionic liquid modified layered double hydroxide", *Ceramics International*, v. 50, n. 14, pp. 26160–26170, 2024. doi: http://doi.org/10.1016/j.ceramint.2024.04.357.

[40] XUE, Y., PANG, X., JIANG, B., *et al*., "Corrosion and corrosion fatigue performances of micro - arc oxidation coating on AZ31B cast magnesium alloy", *Materials and Corrosion*, v. 70, n. 2, pp. 268–280, 2019. doi: http://doi.org/10.1002/maco.201810293.

## SUPPLEMENTARY MATERIAL

The following online material is available for this article:

Figure S1 – Optical micrographs of Vickers microhardness indentations on the MAO coatings prepared at (a) 300 V, (b) 350 V, (c) 400 V, and (d) 450 V.